



## **Simulation of the Penetration of a Sequence of Bombs Into Granitic Rock**

**Tarabay H. Antoun, Ilya N. Lomov, Lewis A. Glenn**

Lawrence Livermore National Laboratory, Geophysics and Global Security Division, Livermore,  
CA 94550

---

### **Abstract**

This computational study was undertaken to investigate the penetration efficiency of a sequence of penetrating bombs into granitic hard rock. The main objective of the study was to ascertain the feasibility of using several bombs — all precision-guided to the same target point and detonated a few tens of milliseconds apart — to defeat a Hard and Deeply Buried Target (HDBT) that cannot be defeated using conventional means. Several simulations were performed in support of this objective, including a sequence of six consecutive bombs traveling with a velocity of 300 m/s, with each bomb being made to penetrate into the crater produced by its predecessor. The simulations were performed using GEODYN — a parallel Eulerian hydrocode with adaptive mesh refinement capabilities — and a constitutive model for granite that was calibrated using ground motion data from several underground explosions. The cumulative penetration depth from all six bombs was 5.7 m, with the first bomb penetrating as much as 2.1 m and the last one penetrating as little as 0.4 m. The general trend of decreasing penetration depth with each successive bomb was shown to be primarily attributed to crater geometry and to accumulation of high strength steel in the bottom of the crater. Shock conditioning of the rock was shown to have a favorable effect on penetration.

© 2003 Published by Elsevier Ltd.

**Keywords:** multiple penetration, simulation, GEODYN, effect of crater geometry, effect of shock conditioning,

---

### **1. Introduction**

Deep underground structures are often used by potential adversaries of the United States for storage of weapons of mass destruction (WMD), long-range missiles, and other critical assets. These facilities are also used as sanctuaries for national wartime leaders and as command and control bunkers. The intelligence community suspects with reasonable certainty that there are more than 10,000 Hard and Deeply Buried Targets (HDBT) worldwide, with the number projected to increase over the next 10 years [1]. The proliferation of HDBTs, combined with the lack of effective conventional weapons that are capable of holding such facilities at risk are two of the main reasons why hard and deeply buried target defeat (HDBTD) is a matter of national interest and one of the important challenges facing the defense community.

With conventional weapons, the primary HDBT defeat mechanism is structural damage to the facility caused by the weapon-induced ground shock. One way to enhance the ground shock environment and thereby extend the range of the weapon is to decrease the slant range, between

the weapon and the intended target. Decreasing the slant range leads to less attenuation in the amplitude of the spherically divergent ground shock emanating from the explosion. In turn, this leads to a more severe loading environment applied to the structure. Another way to enhance the ground shock environment is to improve the coupling of the energy released by the weapon into the geologic medium. This can be achieved by increasing the depth of burial. As shown in Fig. 1, the equivalent yield coupling factor (YCF) increases significantly with increasing depth of burial, especially for the first few scaled meters below the ground surface.

Both a decreased slant range and an improved coupling factor can be achieved by causing the detonation to occur deeper underground. In practice, this is difficult to attain because existing conventional weapons are only capable of limited penetration into hard rock targets. Most HDBT facilities are so deep that neither developmental nor existing weapons can penetrate to sufficient depths to directly destroy critical assets. Thus, an innovative approach is required for achieving deeper penetration. One such approach—termed Consecutive Miracles — was born at the Air Force Weapons Laboratory in 1991 [2]. This approach employs penetrating bombs from the current inventory, but significantly changes the tactics of employment. The Defense Threat Reduction Agency (DTRA) demonstrated the feasibility of the Consecutive Miracles concept as far back as 1993 by using existing technology to deliver several precision-guided penetrating weapons, in series, to the same target. The computational study described here further explores this concept as a means of achieving deep penetration into hard rock, and attempts to shed light on the advantages and limitations of the approach.

## 2. Objectives and Approach

This computational study was undertaken to investigate the penetration efficiency of a sequence of bombs into granitic hard rock. The main objective of the study was to investigate the feasibility of using several precision-guided penetrating bombs, in series, to excavate a deep hole in the rock. Several simulations were performed in support of this objective. These simulations are summarized in Table 1, and they include a series — PEN-1A through PEN-6A — consisting of a sequence of six penetrating bombs, each with an initial downward vertical velocity of 300 m/s. The computational domain at the beginning of the simulation is shown in Fig. 2. The first bomb was dropped and allowed to penetrate into a granitic half space until its vertical velocity became negligible (less than 10 m/s), at which time the HE burn sequence was initiated at the tail end of the bomb. Ten milliseconds after detonation, corresponding to 3 m separation between bombs at the time of detonation, a second bomb was dropped into the bottom of the crater. Once again, the HE was detonated only after the forward motion of the projectile had essentially ended. This sequence is illustrated in the logarithm of density plot of Fig. 3, and it was repeated until the response of the granite to all six bombs had been simulated. To better understand the results of this bomb sequence simulation, additional simulations were also performed to help isolate and quantify the effects of those parameters that had a significant effect on penetration.

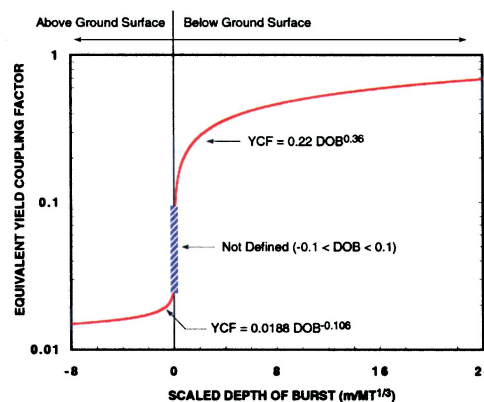


Fig. 1. Equivalent yield coupling factor as a function of scaled depth of burst [3].

The simulations were performed using GEODYN, a parallel Eulerian hydrocode with adaptive mesh refinement capabilities. The Eulerian framework of adaptive mesh refinement (AMR) [4] is a relatively mature technique for dynamically applying high numerical resolution to those parts of a problem domain that require it, while solving less sensitive regions on less expensive, coarser computational grids. In combination, Eulerian Godunov methods with AMR have been proven to produce highly accurate and efficient solutions to shock capturing problems. The method used here is based on some modifications of the single-phase high-order Godunov method, and is described in detail by Lomov and Rubin [5].

Among its many features, GEODYN includes a high order interface reconstruction algorithm, and a unique remapping feature that allows the user to overlay a sub-domain onto an existing grid at any point during the simulation. This remapping option was used during the present investigation to overlay a new bomb onto the computational domain at the conclusion of the previous bomb sequence (see Fig. 3c and 3d).

The simulations were performed on two of LLNL's massively parallel computing platforms: FROST and TC2K. FROST is one of the three IBM RS/6000 SP systems that make up the ASCI (Accelerated Strategic Computing Initiative) White platform. It is comprised of 68 nodes, each consisting of a 16-way symmetric multiprocessor (SMP), for a total of 1088 CPUs. Each CPU operates at 375 MHz and each node has a 1.5 GFlops theoretical peak performance. TC2K is a Compaq Sierra cluster comprised of 128 AlphaServer ES40 nodes with 4 EV67 CPUs per node operating at 667 MHz with 8 MB of cache. TC2K's theoretical peak performance is 681 GFlops.

Table 1. Simulations summary.

<i>Simulation</i>	<i>Brief Description</i>
PEN-1A	First bomb of the six-bomb-sequence simulation
PEN-2A	Second bomb of the six-bomb-sequence simulation
PEN-3A	Third bomb of the six-bomb-sequence simulation
PEN-4A	Fourth bomb of the six-bomb-sequence simulation
PEN-5A	Fifth bomb of the six-bomb-sequence simulation
PEN-6A	Sixth bomb of the six-bomb-sequence simulation
PEN-2B	Same as PEN-2A with the residual steel removed from the bottom of the crater
PEN-2C	Same as PEN-2B with the rock assumed initially undamaged
PEN-H1D	Bomb initially positioned in a hole with a diameter equal to 1 bomb diameter
PEN-H2D	Bomb initially positioned in a hole with a diameter equal to 2 bomb diameter
PEN-H4D	Bomb initially positioned in a hole with a diameter equal to 4 bomb diameter
PEN-H8D	Bomb initially positioned in a hole with a diameter equal to 8 bomb diameter

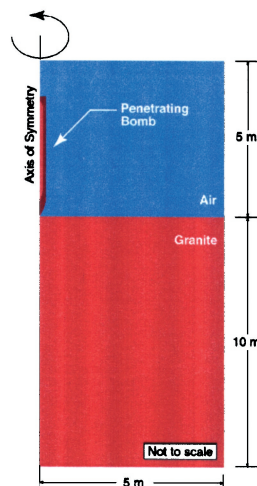


Fig. 2. Schematic of the computational domain at the beginning of the six-bomb-sequence simulation.



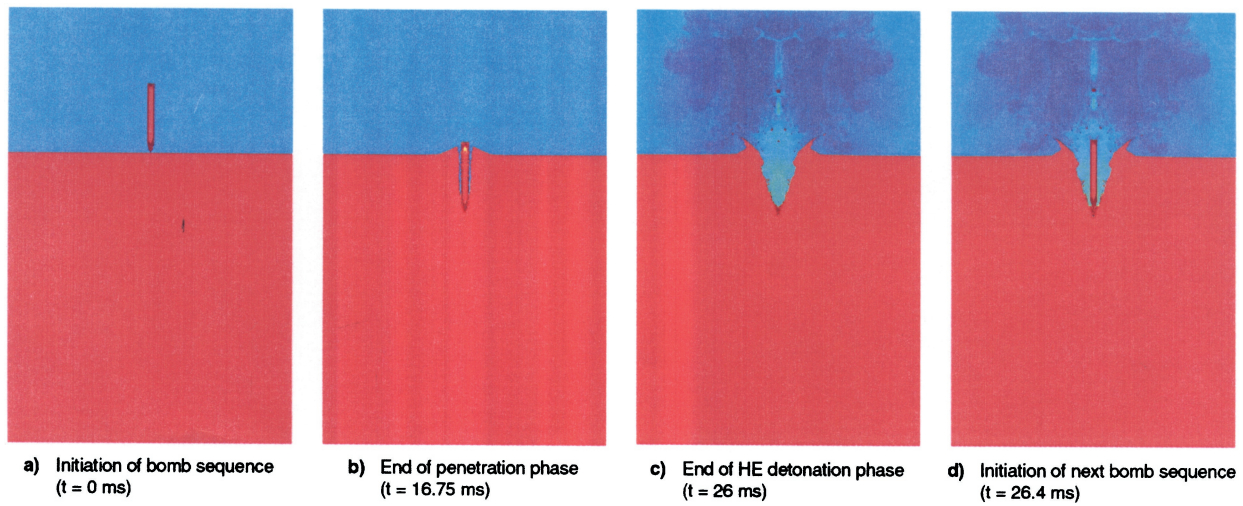


Fig. 3. Logarithm of density plots illustrating the sequence of events associated with a typical penetration event.

### 3. Granite Model

The constitutive model used to describe the dynamic response of granite in the present investigation is nonlinear, thermodynamically consistent, and properly invariant under superposed rigid body motions [6]. The model equations are valid for large deformation and they are hyperelastic in the sense that the stress tensor is related to a derivative of the Helmholtz free energy. The material is assumed to be initially isotropic and the mathematical structure of plasticity theory is applied to capture the basic features of the mechanical response.

The model accounts for the effects of scaling, bulking, yielding, material damage, and porous compaction on the material response. The deviatoric behavior of the rock is described using an elastic-viscoplastic model, coupled with a damage model, and the volumetric behavior is described using an equation of state, coupled with a porous compaction and bulking model. Initial yielding is followed by a plastic strain hardening phase that persists until the loading path intersects the failure surface. Thereafter, damage accumulation causes gradual strength reduction from the failure surface down to a residual value equivalent to a small fraction of the undamaged strength.

#### 3.1 Strength Model

As described in Rubin et al. (2000) [6], the physical phenomena that influence the yield strength  $Y$  are taken into account using a multiplicative form with  $Y$  given by:

$$Y = Y_0 F_0(\xi, p) F_1(\xi, p) F_2(\epsilon_p) F_3(\rho, \epsilon) \quad (1)$$

where  $Y_0$  is the initial yield strength of the rock at zero pressure, the functions  $F_0$ ,  $F_1$ ,  $F_2$ , and  $F_3$ , respectively account for the effects of scaling, hardening, damage and melting on the strength and failure of the rock.

In Equation 1,  $F_0$  is a scaling function equal to unity for intact rock samples and decreases monotonically as a function of pressure and inelastic deformation. This function was incorporated into the model because our simulation results showed that the yield and failure stresses measured statically using relatively small, defect-free samples had to be reduced to satisfactorily reproduce the dynamic data. This is in line with experimental observations that show the strength of granite and other geologic materials to decrease with increasing specimen dimensions.

$F_1$  is a hardening function expressed in terms of the hardening parameter  $\xi$  as follows:



$$F_1 = \{1 + (k_1(p) - 1)\xi\} f_1(p) \quad (2)$$

where  $k_1$  is a function that expresses the relationship between the initial yield and the failure strength of the rock, both of which are varying functions of pressure. The hardening parameter  $\xi$  varies between 0 and 1; it is determined by an evolution equation of the form

$$\dot{\xi} = k_2 \dot{\epsilon}_p (1 - \xi) / f_1(p) \quad (3)$$

where  $\dot{\epsilon}_p$  is the plastic strain rate and  $k_2$  is a model parameter. The pressure hardening function  $f_1(p)$ , which expresses the dependence of the yield strength on applied pressure, is determined from laboratory measurements on small rock samples (e.g., [7]). In the code,  $f_1(p)$  can be specified as an analytic function fitted to the experimental data, or it can be determined by interpolation from a set of tabular data.

The damage function  $F_3$  controls the strength degradation of the rock after damage begins to accumulate. It is expressed in terms of the plastic strain,  $\epsilon_p$ , using the simple relation

$$F_2 = \max \begin{cases} 1 - k_5 \epsilon_p & (4a) \\ \alpha p / Y(p) & (4b) \end{cases} \quad (4)$$

where  $k_5$  and  $\alpha$  are model parameters, and  $Y(p)$  is the pressure-dependent, but undamaged value of the yield strength. The function in Equation (4a) takes on values ranging between 1 for the intact material, and 0 for the fully damaged material. The function in Equation (4b) represents the residual strength of the damaged material. It is a linear function of pressure and it represents only a small fraction of the strength of the undamaged rock. The parameter  $\alpha$  in this equation can be viewed as the friction coefficient of the damaged material. A value of  $\alpha=0.1$  was used in the simulations discussed here.

$F_3$  models the effect of material melting (i.e., thermal softening) and is expressed in terms of the ratio of the specific energy,  $\epsilon$ , to the density-dependent specific melting energy,  $\epsilon_m(\rho)$ , using the following relation:

$$F_3 = 1 - \min \left\{ 1, \frac{\epsilon}{\epsilon_m(\rho)} \right\}. \quad (5)$$

### 3.2 Porous Compaction and Bulking

The equation of state, which describes the solid rock behavior, is supplemented with an analytic porous compaction model that describes the relationship between pressure and porosity. Also included in the volumetric behavior description is a dilatancy model that relates bulking to plastic distortion in such a way as to ensure thermomechanical consistency with the second law of thermodynamics.

The total gas porosity is separated into two parts,  $\phi_1$  and  $\phi_2$

$$\phi = \phi_1 + \phi_2 \quad (6)$$

$\phi_1$  describes changes in porosity associated with the compaction of existing pores, whereas  $\phi_2$  describes changes in porosity associated with bulking and it is proportional to the rate of dissipation due to plastic deformation.

The evolution of the porosity component  $\phi_1$  is described using the relation,

$$\dot{\phi}_1 = -\Gamma_c \langle \phi_1 - \phi_c^* \rangle \quad \text{for } p > p_c \quad (7)$$

where  $\Gamma_c$  is a model parameter, and  $\phi_c^*$  is the static equilibrium porosity associated with the current compressive pressure (i.e., in the absence of rate effects,  $\phi_1 = \phi_c^*$ ). The dependence of  $\phi_c^*$  on volume and porosity is expressed by the relation,

$$\phi_c^* = \begin{cases} \Phi_1 & \text{for } 1/J < 1/J_c \\ \Phi_1 - c_1(1-\Phi) \left[ \frac{1}{J} - \frac{1}{J_c} \right] & \text{for } 1/J_c < 1/J < c_2/J_c \\ \bar{\phi}_c \exp \left[ \left( c_1(1-\Phi) \left\langle \frac{1}{J} - \frac{c_2}{J_c} \right\rangle \right) / \bar{\phi}_c \right] & \text{for } c_2/J_c < 1/J \end{cases} \quad (8)$$

where

$$\bar{\phi}_c = \Phi_1 - c_1(1-\Phi) \left[ \frac{c_2}{J_c} - \frac{1}{J_c} \right], \quad (9)$$

$\Phi_1$  is the value of the porosity  $\phi_1$  in the reference configuration,  $J = \rho_o/\rho$  is the Jacobian of the deformation tensor,  $\Phi$  is the total porosity in the reference configuration, and,  $c_1$  and  $c_2$  are model parameters subjected to the following constraints:

$$0 \leq c_1 \leq 1 \quad 1 \leq c_2 \leq 1 + \frac{\Phi_1 J_c}{c_1(1-\Phi_1)}. \quad (10)$$

$J_c$  is the critical value of  $J$  beyond which compaction occurs. It is determined from the following expression,

$$\frac{1}{J_c} = \frac{p_c}{(1-\Phi)\rho C^2} + \left( \frac{1-\Phi_1-\phi_2}{1-\Phi} \right) \left\langle 1 - \frac{\Gamma \mathcal{E}}{C^2} \right\rangle \quad (11)$$

in which  $\mathcal{E}$  is the specific energy (energy per unit mass),  $C$  is the bulk sound speed, and  $\Gamma$  is the Grüneisen coefficient.

The evolution of the porosity component  $\phi_2$ , which models the porosity due to bulking, is described using the following relation.

$$\dot{\phi}_2 = (1-\phi) H(\phi_2) \left[ \frac{m_d \sigma_{eff} \dot{\epsilon}_p \langle \phi^* - \phi_2 \rangle}{\max(\phi^*, p)} - m_c (1-F_2) \langle -D \cdot I \rangle \right] \quad (12)$$

In this equation,  $\sigma_{eff}$  is the effective, or von Mises stress and  $\dot{\epsilon}_p$  is the effective plastic strain rate.  $\phi^*$  is a model parameter that specifies the maximum bulking porosity that can be achieved,  $m_d$  determines the rate of bulking and  $m_c$  is used to control the rate of re-compaction of the bulking porosity, a process that takes place only when the material is damaged and accelerates as damage increases and  $F_2 \rightarrow 0$ . The rate at which bulking may proceed is constrained by the second law of thermodynamics, which governs the entropy production of dissipative thermodynamic processes.

The model has been calibrated using both static laboratory data and ground shock measurements from several underground explosions, including velocity and displacement waveforms from PILE DRIVER, a deeply buried underground nuclear explosion detonated in granite at the Nevada Test Site [8]. The calibrated model is capable of predicting, within a factor

of  $\pm 2$ , the peak velocity and peak displacement from tamped explosions in granitic rock over a span of ten orders of magnitudes in explosive yield (Fig. 4).

#### 4. Bomb Model

The bomb model used in the present investigation is shown in Fig. 5. As shown, this 750-kg penetrator is 2.4 m long, and has a 25.4 cm diameter. The case walls are assumed to consist of Vascomax 250 steel, the mechanical response of which is described in the simulations using the Steinberg model [9]. The response of the high explosive is simulated using a JWL equation of state.

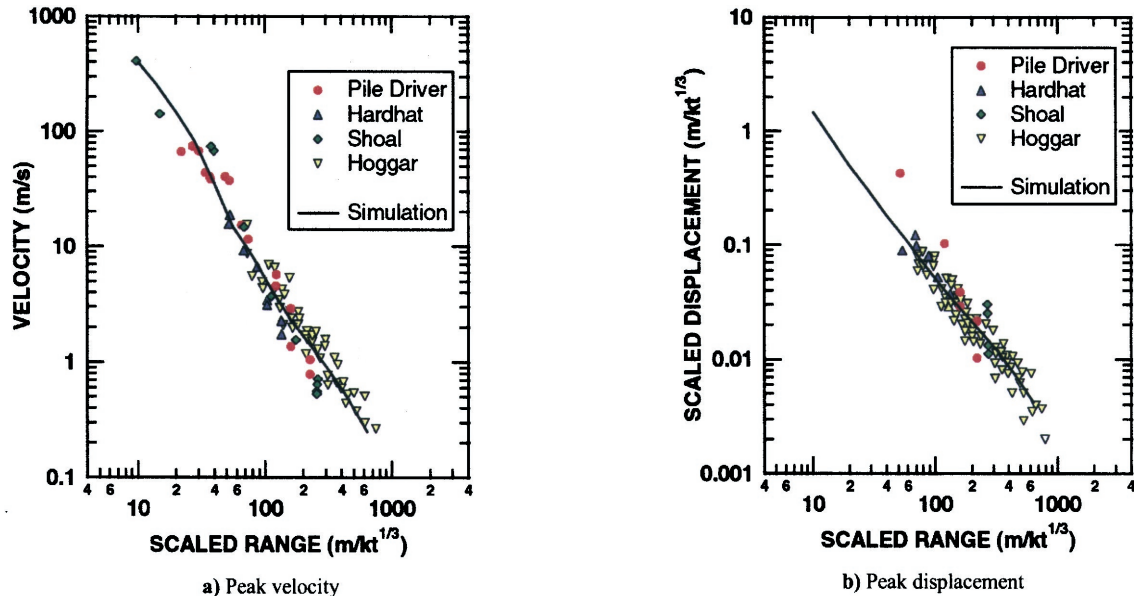


Fig. 4. Comparison of simulated peak velocity and peak displacement attenuations with measurements in granite.

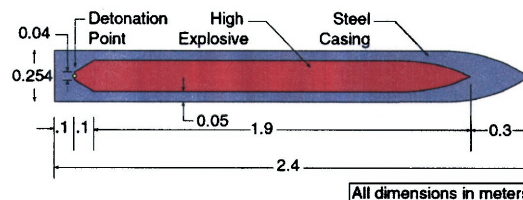


Fig. 5. Bomb model used in the simulations.

#### 5. Simulation Results

Figure 6 summarizes the penetration history from all six penetrators in the six-bomb-sequence simulation. The figure also shows the times corresponding to the initiation of each penetration event as well as the times corresponding to the detonation of the HE in each bomb. Each of the six segments of the penetration history curve corresponds to one of the bombs that made up the complete sequence.

As shown in the figure, appreciable increase in the depth of the crater occurs only during the penetration phase of each bomb cycle. The increase in crater depth during the HE detonation phase is barely perceptible. Indeed, a small decrease in penetration depth is observed in some instances during the HE detonation phase. This rebound is negligibly small and it occurred primarily when the stresses were allowed to relax for longer than 10 ms after the detonation of the HE, as in Simulation PEN-2A and PEN-6A. In contrast, the width of the crater increases appreciably only during the HE detonation phase of the bomb cycle, and remains essentially constant during the penetration phase of the cycle.

In addition to widening the crater, the HE detonation also helps ensure that the crater remains



free of bomb debris and rock fragments. The high-pressure detonation process leads to a turbulent upward flow of detonation products that entrains the debris and fragments, depositing them later either along the crater sidewalls or in the atmosphere outside the crater.

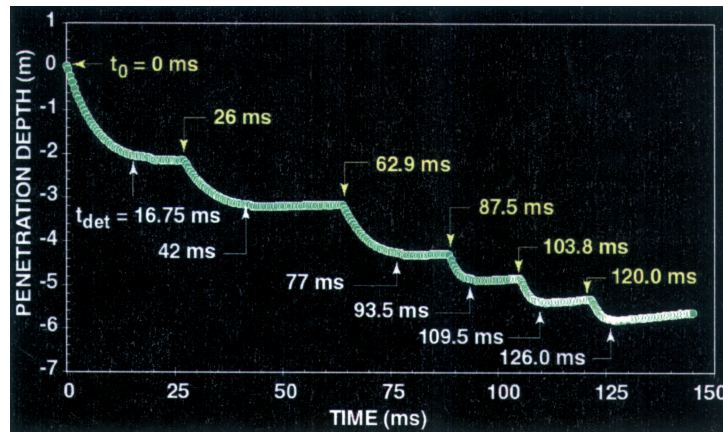


Fig. 6. Summary of the penetration histories from the six-bomb-sequence simulation.

Both the penetration phase and the detonation phase play important roles in advancing the hole excavation process. However, the two phases must be synchronized in a way that maximizes penetration and minimizes adverse interaction effects. For instance, detonating the HE before the bomb comes to a stop would have an adverse effect on penetration depth. Initiating the penetration phase of a new bomb cycle too soon after the detonation of the HE from a previous bomb would have a similarly adverse effect. A 10 ms delay was used in the present study to separate the HE detonation time from the initiation of the next bomb cycle. Combined with the 300 m/s bomb velocity, this delay represents a 3 m separation between bombs at the time of detonation. This delay was chosen to provide sufficient time for the high detonation pressure to attenuate, and the debris to clear out of the crater, thereby reducing the risk of damaging the bomb casing, or causing the bomb to veer off its flight path. The pressure levels prevalent in the crater 10 ms after HE detonation are on the order of 10 bars, negligible compared to the 15.6 kbar yield strength of the steel casing.

### 5.1 Effect of Steel Accumulation in the Crater

Figure 7 shows the crater shape 20 ms after detonation of the HE in the sixth and final penetrator. The penetration depth from each of the 6 bombs is indicated in the figure along with the cumulative total penetration. As shown, the cumulative total penetration depth is 5.7 m, with the first bomb penetrating as much as 2.13 m and the last one penetrating as little as 0.42 m. The data shown exhibit a trend of decreasing penetration depth with each successive bomb. This trend is further illustrated in Fig. 8 where the penetration depth from each of the six penetration events is shown along with the corresponding thickness of residual steel accumulated in the bottom of the crater. This figure appears to show a correlation between the decrease in penetration depth and an increase in the residual steel thickness. This is not a surprising trend since both the density and strength of the bomb casing steel are several times larger than their granite counterparts. Strength and density are known to be among the most important parameters that control penetration response.

A new simulation — PEN-2B — was performed to isolate the effect of steel accumulation on the penetration response. This new simulation is identical to Simulation PEN-2A in all respects except that the residual steel accumulated in the bottom of the crater at the beginning of Simulation PEN-2A (see Fig. 9) was removed before initiating the penetration sequence of Simulation PEN-2B. Figure 10 compares the penetration histories from Simulations PEN-2A and PEN-2B. Although the two curves exhibit similar overall trends, the figure shows that penetration proceeds with greater efficiency in Simulation PEN-2B than it does in Simulation PEN-2A, especially at early times when the penetrator in Simulation PEN-2A is interacting with

the residual steel in the bottom of the crater. The 1.59-m penetration depth achieved in Simulation PEN-2B is 54% greater than the 1.03-m penetration achieved in Simulation PEN-2A.

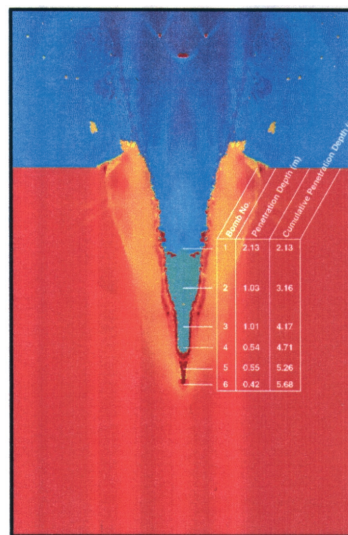


Fig. 7. Crater shape 20 ms after detonation of the HE in the sixth and final penetrating bomb.

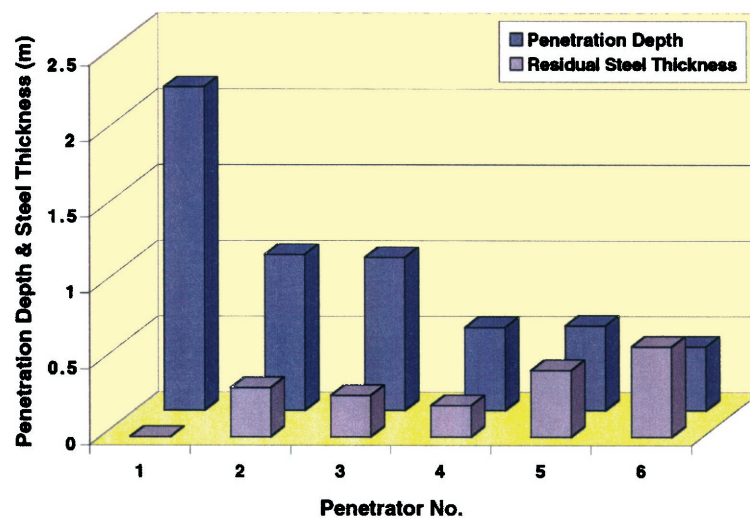


Fig. 8. Penetration depth and corresponding thickness of residual steel from each of the six penetration events.

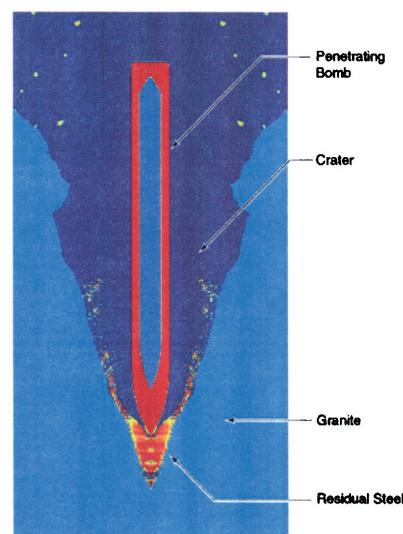


Fig. 9. Density plot of the crater at the beginning of simulation PEN-2A.

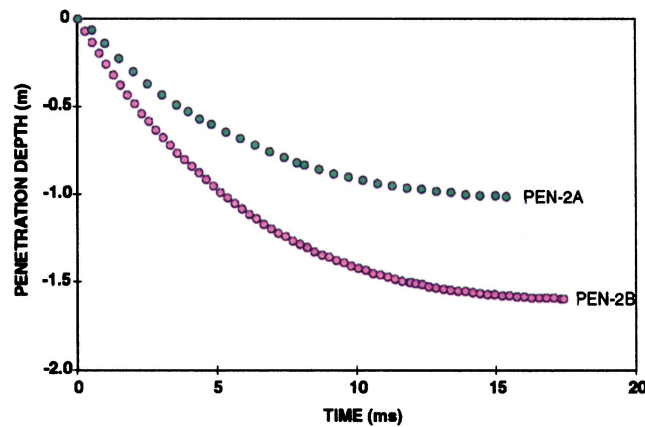


Fig. 10. Effect of the residual steel accumulated in the bottom of the crater on penetration.

This aspect of the simulation results should be investigated further to determine whether the accumulation of steel in the bottom of the crater is a realistic phenomenon, or an artifact related to the limitations imposed on the problem by the use of 2D axisymmetric simulations. All the bombs in the simulations were centered at the axis of symmetry, and they all followed precisely the same flight path. Spatial staggering of successive bombs, even by a few centimeters, might be sufficient to alleviate the steel accumulation problem. Investigating this phenomenon requires the use of 3D simulations; although these are feasible with the GEODYN code, they require considerably more computational resources and are consequently beyond the scope of the present investigation.

## 5.2 Effect of Shock Conditioning of the Rock

The constitutive model used to describe the response of granite includes effects like pressure and strain hardening, which tend to make it more difficult to penetrate into the rock, as well as damage softening effects, which tend to make penetration easier. Strong interactions among these competing mechanisms make it difficult to determine whether shock conditioning of the rock during one bomb cycle causes an increase or a decrease in the penetration depth achieved during subsequent bomb cycles. To address this question, Simulation PEN-2C was performed with the objective of investigating the effect of shock conditioning on the penetration response. The geometry and boundary conditions used in the simulation are identical to those used in Simulation PEN-2B. Whereas the granite in Simulation PEN-2B was preconditioned by the shock loading from the previous bomb cycle, the granite medium in Simulation PEN-2C was assumed to have virgin material properties. The penetration histories from these two simulations are shown in Fig. 11. The results indicate that shock conditioning has a strong favorable effect on the penetration response. Significant differences are observed both in the duration of the penetration event, which varied from 17.4 ms in PEN-2B to 5.96 ms in PEN-2C, and in penetration depth, which varied from 1.59 m in PEN-2B to 0.56 m in PEN-2C.

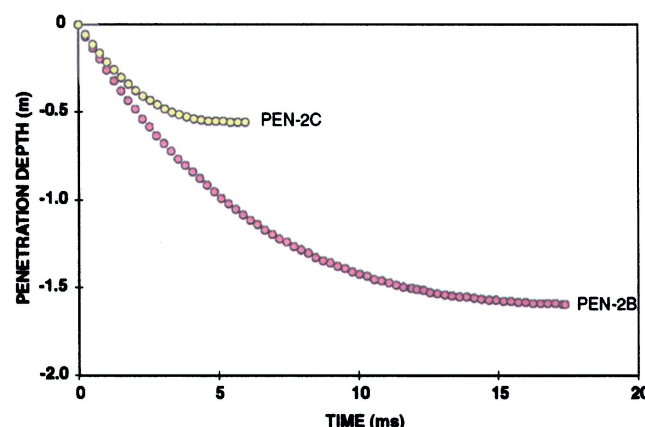


Fig. 11. Effect of shock condition on penetration.



### 5.3 Effect of Crater Geometry

Of all the parameters that were investigated for their influence on the penetration response, crater geometry was found to have the most significant effect. This effect can be quantified by comparing the results of Simulations PEN-1A and PEN-2C. These two simulations are similar in all respects except that in PEN-1A, the penetration event took place near the ground surface, whereas in PEN-2C the penetration event took place in the bottom of the crater left behind from a previous explosion. A comparison of the penetration histories from these two simulations is shown in Fig. 12. Significant differences are observed both in the duration of the penetration event, which varied from 16.75 ms in PEN-1A to 5.96 ms in PEN-2C, and in the total penetration depth achieved, which varied from 2.05 m in PEN-1A to 0.56 m in PEN-2C.

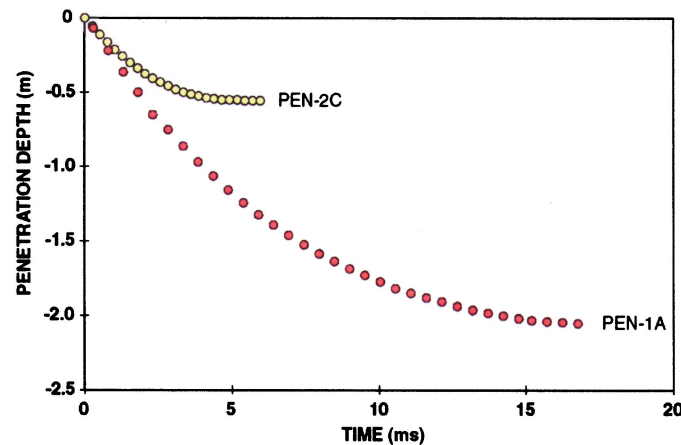


Fig. 12. Effect of the crater geometry on penetration.

Additional simulations were performed to shed more light on the reasons why crater geometry had such a large effect on penetration. Those simulations are labeled PEN-H1D through PEN-H8D in Table 1. In each simulation, the bomb was placed in a hole the diameter of which was an integer multiple of the 254-mm bomb diameter. The hole diameter varied from one bomb diameter in Simulation PEN-H1D to eight bomb diameters in Simulation PEN-H8D. Simulation results are summarized in Figs. 13 through 15. In Fig. 13, the total penetration depth from each of the four simulations is plotted as a function of hole diameter. The horizontal line at a penetration depth of 2.03 m corresponds to the total penetration from Simulation PEN-1A, which in essence represents an infinitely wide hole, and therefore places an upper bound on penetration depth. The data shown in Fig. 13 indicates that penetration depth decreases with decreasing hole diameter, with the most severe decline occurring when the hole size is less than four bomb diameters. Figure 14 shows the crater at the end of three simulations each with a different hole diameter ranging in size from 2 to 8 bomb diameters. When the hole diameter is large, as in part (a) of the figure, a layer of air separates the bomb casing from the rock. In contrast, when the hole diameter is small, as in part (c) of the figure, no air gap is observed between the bomb casing and the rock.

As mentioned above, a precipitous decline in penetration depth begins to occur when the hole size is less than four bomb diameters. The hole size in Fig. 14(b) is four bomb diameters. As shown, this hole size represents a transition from a situation where the hole diameter is relatively large, and the casing is separated from the rock by an air gap; to one where the hole diameter is relatively small and the two are in intimate contact.

To understand the underlying mechanisms that lead to the observed variations in penetration depth, we begin by examining the evolution of the penetration process. As the bomb penetrates into the rock medium, material is displaced away from the flight path of the projectile. A small portion of the displacement is accommodated elastically and by porous compaction; the remainder is accommodated by plastic deformation. The distortion associated with the accumulation of plastic strain also causes bulking and damage. In order for the penetration to proceed efficiently, the material displaced by the penetrator, which now has an increased volume

due to bulking and a reduced yield strength due to damage, must be transported away from the region near the tip of the penetrator. The results of Fig. 14 show that it is easier to transport material out of the crater when the hole diameter is relatively large than it is when the hole diameter is relatively small. In a large diameter hole, the rock/air interface in the bottom of the hole provides a free surface that relieves the stresses in the midst of the rock mass. Furthermore, the upward motion of the ground surface in the bottom of the hole (see Fig. 14(a)), provides space for the material displaced from the path of the projectile to occupy. In contrast, a small diameter hole does not provide sufficient free surface for stress release, nor does it allow space for displaced material to occupy. Consequently, the pressure in the rock ahead of the penetrator increases with decreasing hole diameter. The higher pressure also causes the yield strength to increase because the rock strength is pressure dependent.

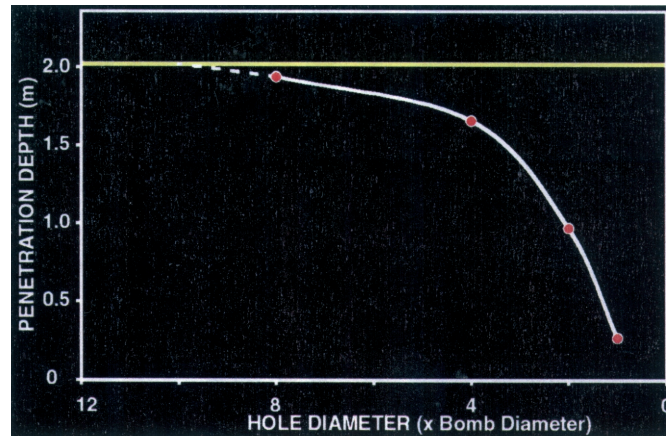


Fig. 13. Effect of hole size on depth of penetration.

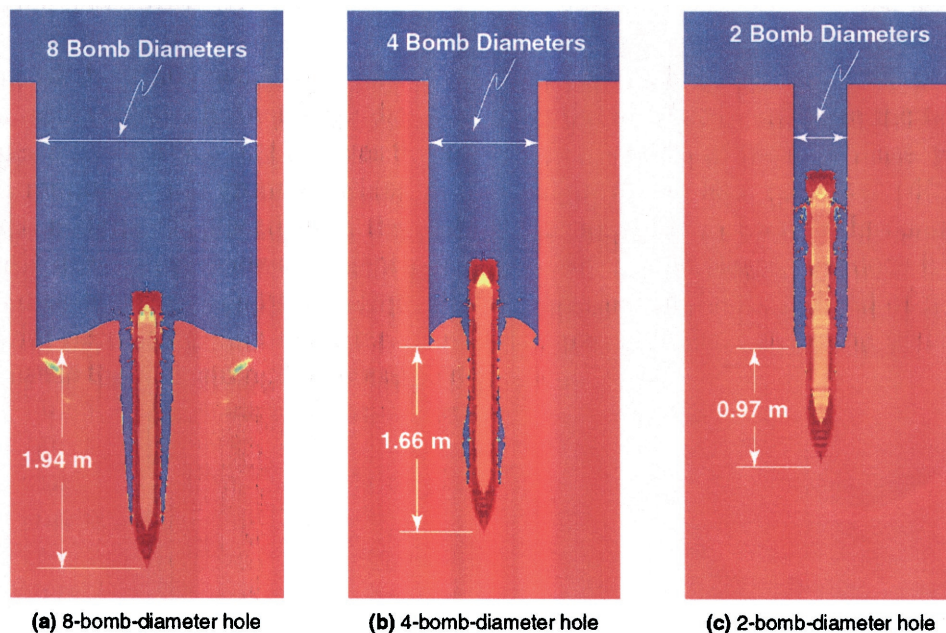


Fig. 14. Density snapshots taken as the penetrator comes to a stop in simulations with three different hole sizes.

Figure 15 shows the pressure and yield strength distributions in the rock in the vicinity of the penetrator for the three hole diameters shown in Fig. 14. Figs 15(a-c) correspond to the midpoint of the penetration event, when the velocity of the penetrator is 150 m/s, or one half the initial velocity. Figs. 15(d-f) correspond to the end of penetration, when the penetrator velocity becomes negligible (less than 10 m/s). Both these figures show that the pressure and yield strength ahead of the penetrator are inversely proportional to hole diameter. As a result, the resistance of the rock to penetration is also inversely proportional to hole diameter: the smaller the hole diameter the higher the resistance to penetration.



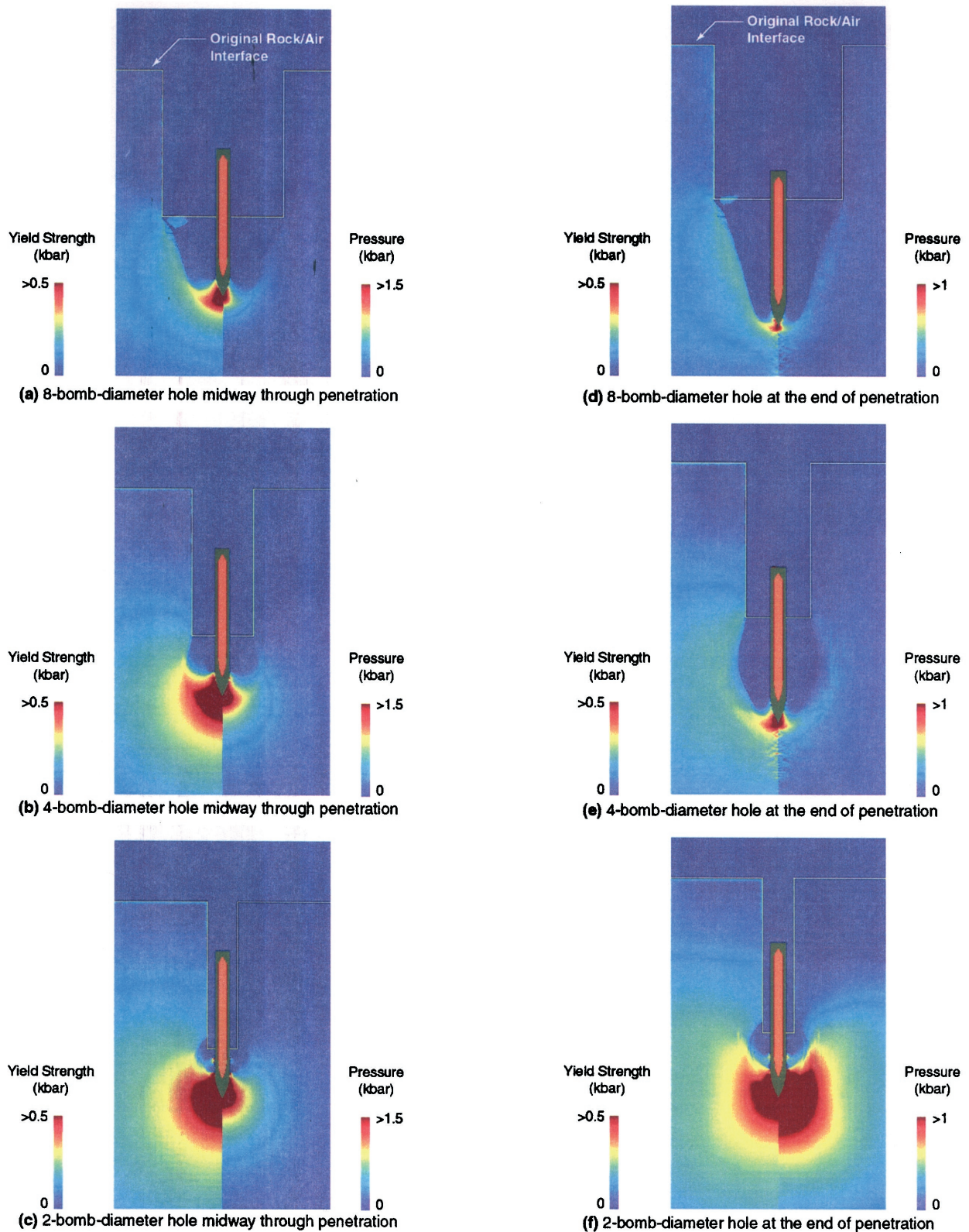


Fig. 15. Yield strength and pressure distributions in the rock in simulations with three different hole sizes.

## 6. Summary and Conclusions

This study investigated the feasibility of using six precision-guided penetrating bombs, in series, to excavate a deep hole in granitic rock. The cumulative penetration depth from all six bombs was 5.7 m, with the first bomb penetrating as much as 2.1 m and the last one penetrating as little as 0.4 m. The general trend of decreasing penetration depth with each successive bomb was shown to be primarily attributed to crater geometry and to accumulation of high strength



steel in the bottom of the crater. Shock conditioning of the rock was shown to have a favorable effect on penetration.

Removal of the residual steel from the bottom of the crater led to a factor of 1.54 increase in penetration depth. The accumulation of residual steel in the bottom of the crater could be an artifact related to the limitations imposed on the problem by the use of 2D axisymmetric geometry. This is why three-dimensional simulation would need to be performed to determine whether spatial staggering of the bomb in the bottom of the crater could help alleviate the steel accumulation problem, and lead to more efficient penetration toward the later stages of the bomb sequence.

Penetration depth in shock-conditioned granite was 2.8 times greater than it was in virgin rock. This is a large effect that also requires further investigation to clarify matters. To this end, a methodical parameter sensitivity study could be performed, wherein various aspects of the material response (i.e., bulking, damage, hardening, etc.) can be isolated and their effect on penetration can be quantified.

Of all the parameters that were investigated for their influence on the penetration response, crater geometry was found to have the most significant adverse effect. When the penetration event took place near the ground surface, the simulated penetration depth was 3.8 times greater than its counterpart when the penetration event took place in the bottom of the crater. Additional simulations established a correlation between the width of the crater and penetration depth, suggesting that widening the crater should help alleviate the problem. One way this might be achieved is by alternating penetrating bombs that have a relatively low HE to total mass ratio (on the order of 1:8), with conventional bombs that have a much higher ratio (usually on the order of 1:2).

## Acknowledgments

This work was performed under the auspices of the U.S. Department of Energy by the University of California, Lawrence Livermore National Laboratory (LLNL) under contract No. W-7405-Eng-48. The study was inspired by Jim Hammer, X Division, LLNL.

## References

- [1] Report to Congress on the Defeat of Hard and Deeply Buried Targets, submitted by the Secretary of Defense in Conjunction with the Secretary of Energy (2001).
- [2] Henny RW., Babcock SM., Renick JD., "Consecutive miracles," 9<sup>th</sup> International Symposium on Interaction of the Effects of Munitions with Structures, Berlin-Strausberg, Germany (May, 1999).
- [3] Drake JL., Blouin SE., Smith EB., "Ground shock beneath near surface explosions – the DUG methodology," Draft Technical Report, Applied Research Associates, Albuquerque, NM (1988).
- [4] Berger MJ., Colella P., "Local adaptive mesh refinement for shock hydrodynamics," *J. Comp. Phys.*, **82**(1), 64–84 (1989).
- [5] Lomov I., and Rubin M., "Numerical simulation of damage using an elastic-viscoplastic model with directional tensile failure," to be published in the proceedings of DYMAT 2003, Porto, Portugal (2003).
- [6] Rubin MB, Vorobiev OYu., Glenn LA., "Mechanical and numerical modeling of a porous elastic-viscoplastic material with tensile failure," *Int. J. Solids and Structure*, **37**, 1841–1871 (2000).
- [7] Schock RN., Heard HC., and Stephens DR., "Stress-strain behavior of a granodiorite and two graywackes on compression to 20 kilobars," *J. Geophys. Res.*, **78** (36), 5922–5941 (1973).
- [8] Antoun TA., Lomov IN., and Glenn LA. "Development and application of a strength and damage model for rock under dynamic loading," Proceedings of the 38<sup>th</sup> U.S. Rock Mechanics Symposium, Rock Mechanics in the National Interest, Edited by D. Elsworth, J. Tinucci, and K. Heasley, A.A. Balkema Publishers, Lisse, The Netherlands, 369–374 (2001).
- [9] Steinberg DJ. "Equation of state and strength properties of selected materials," University of California, Lawrence Livermore National Laboratory, Report UCRL-MA-106439 (1991).